Materials & Design 263 (2026) 115652

Contents lists available at ScienceDirect

Materials & Design

journal homepage: www.elsevier.com/locate/matdes

Microwave-assisted synthesis of ZIF-67(Co)-based composite for efficient separation of oils and organic contaminants from water

Georgy Givirovskiy[a,*], Daria Givirovskaia[a], Yerkezhan Yerkinbekova[a], Ville Laitinen[a], Liisa Puro[a], Timo Laakso[a], Sari Granroth[b], Ermei Mäkilä[b], Eveliina Repo[a]

[a] School of Engineering Science, LUT University, Lappeenranta 53850, Finland
[b] Department of Physics and Astronomy, University of Turku, Turku FI-20014, Finland

HIGHLIGHTS

- A rapid two-step microwave-assisted synthesis enables a hierarchical MOF-based composite on carbon fibers.
- The designed architecture combines nanoscale crystalline domains with interconnected porous pathways.
- The hierarchical surface structure induces superhydrophobic and superoleophilic wettability.
- The composite exhibits high sorption capacity and reusability for oil and organic contaminant removal from water.

GRAPHICAL ABSTRACT

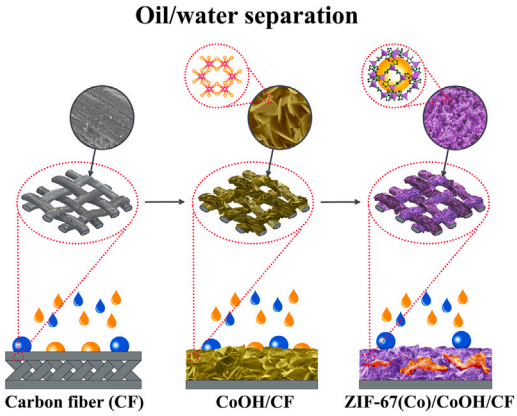

ARTICLE INFO

Keywords:
Metal-organic frameworks
ZIF-67
Microwave-assisted synthesis
Hydrophobic sorbents
Oil/water separation
Environmental remediation

ABSTRACT

Oil pollution and industrial organic contaminants pose risks to aquatic ecosystems and human health, creating a need for sorbent materials that combine high efficiency, selectivity, and durability. Herein, we report a hierarchical metal-organic framework-based composite sorbent prepared via a rapid two-step microwave-assisted strategy. In the first step, cobalt hydroxide nanosheet arrays were uniformly grown on fluorine-modified carbon fibers using a pulsed microwave-assisted approach, enabling ultrafast nanostructure formation. In the second step, zeolitic imidazolate framework-67 nanocrystals were deposited onto the nanosheets, yielding a hierarchical architecture with nanoscale crystallites and microporosity. The composite exhibited a transition from hydrophobic/oleophilic to superhydrophobic/superoleophilic behavior, enabling efficient and selective oil/water separation. Sorption tests revealed high uptake capacities (84–321 wt.%) across a broad range of organic liquids, surpassing many previously reported metal-organic framework-based sorbents. The composite also enabled the treatment of surfactant-stabilized oil-in-water emulsions, achieving ~76% diesel removal within 30 minutes. Moreover, the material demonstrated excellent reusability and stability under repeated cycling and harsh experimental conditions, retaining both structural integrity and sorption performance. The developed synthesis strategy enables rapid fabrication of highly efficient sorbents for environmental remediation and provides experimental insights broadly relevant for the design of other metal-organic framework-derived composites with hierarchical structures.

* Corresponding author.
Email address: Georgy.Givirovskiy@lut.fi (G. Givirovskiy).

https://doi.org/10.1016/j.matdes.2026.115652
Received 11 November 2025; Received in revised form 1 February 2026; Accepted 11 February 2026
Available online 13 February 2026
0264-1275/© 2026 The Authors. Published by Elsevier Ltd. This is an open access article under the CC BY license (http://creativecommons.org/licenses/by/4.0/).

1. Introduction

Despite advancements in the safety of crude oil extraction and transportation, oil spills and associated chemical leakage accidents continue to pose significant threats to marine and coastal ecosystems [1–3]. These environmental disasters, exacerbated by rapid industrial development and expanding offshore petroleum activities, have caused severe ecological damage, economic losses, and a growing global focus on effective cleanup strategies [4,5]. Current conventional techniques for oil/water separation primarily rely on physical treatment methods [6] alongside chemical and biological remediation approaches [7,8]. Although effective to some extent, conventional techniques are often hindered by challenges like high energy consumption, limited selectivity, and inefficiency in managing complex oil/water mixtures, underscoring the demand for complementary or performance-enhancing technologies. In this context, material-based approaches [9], particularly the separation of oil using porous materials, are emerging as a promising and innovative research direction [10].

Over the past years, various advanced porous materials have been developed for efficient oil/water separation, including carbon-based materials [11,12], bio-based materials [13], 3D-structured porous materials [14,15], polymeric materials [16,17], as well as diverse nanomaterials and their composites [18,19]. Despite the rapid development of diverse porous sorbents, achieving a balanced combination of high separation efficiency, selective wettability, and long-term mechanical robustness remains a major challenge in the field [10,20,21]. In practice, porous materials for oil/water separation often face a fundamental engineering conflict, where optimization of one performance metric is achieved at the expense of others. Specifically, increasing a material's porosity to enhance adsorption efficiency typically compromises its mechanical strength and structural durability [22,23]. Furthermore, achieving high selectivity through nanometer-level pore control or dense surface functionalization may lead to reduced permeability or limited overall adsorption capacity [24]. These intrinsic trade-offs highlight that further improvements in oil/water separation performance require rational structural design of sorbent materials rather than incremental material substitution.

Amid ongoing progress in sorption material development, metal-organic frameworks (MOFs), a class of crystalline porous materials, have garnered significant scientific attention, emerging as a rapidly growing research field with a broadening range of proposed applications [25–27]. The growing interest in MOFs is primarily driven by their remarkable properties, including exceptionally high surface areas and porosity, structural tunability, and precisely controllable physical and chemical characteristics [28,29]. From the perspective of oil/water separation, the high surface area and porosity of MOFs greatly enhance sorption performance by providing numerous accessible sites for effective molecular interactions and diffusion [30]. Moreover, structural tunability enables the design of MOF-derived sorbents with dual functionalities, such as hydrophobicity to repel water and oleophilicity to selectively capture oil, or vice versa [9,30,31]. These unique attributes are critical for effective oil removal, establishing MOFs as a promising platform for creating materials specifically tailored for oil/water separation [30,32,33].

Zeolitic imidazolate frameworks (ZIFs), a subclass of MOFs, are porous crystalline materials characterized by zeolite-like structures formed from tetrahedral metal ions and imidazolate ligands [34]. ZIFs offer permanent porosity and high thermal and chemical stability [35], which make them particularly attractive for oil/water separation applications [36]. In the structure of ZIFs, metal ions mimic the role of silicon, while imidazolate anions form bridges analogous to oxygen's role in zeolites [34]. As a result of their unique structural features, ZIFs can adopt numerous three-dimensional topological structures [37], and it is anticipated that ongoing research will uncover new topologies with superior functionalities in the foreseeable future [38]. Among different well-studied ZIFs, ZIF-8 and ZIF-67 with metal centers composed of Zn^{2+} and Co^{2+} ions, respectively, have piqued vast attention as prospective oil sorbents [36,39]. However, the direct use of ZIFs in powder form is limited by issues such as poor recoverability, reduced recyclability, and insufficient sorption capacity [30]. To address these challenges, recent studies have focused on incorporating ZIFs onto high-surface-area substrates, such as metal meshes [40,41], melamine sponges and foams [42–45], polymer matrices [46], and nanofibers [47–49], to create composite materials with superior oil-removal efficiency.

Regardless of the substrate used, most published studies focus on the direct in situ growth of ZIFs by immersing a substrate in a solution containing metal ions and an organic linker [44,48,50]. The synthesis is typically carried out at room temperature [44,48] or under elevated temperatures using hydrothermal or solvothermal methods in autoclaves [43]. Despite being a simple and effective approach, the direct in situ growth method has certain drawbacks, including uneven substrate coating [44], particle agglomeration [46], weak adhesion [51], slow growth kinetics [52], and limited control over the morphology and thickness of the ZIF layer [53]. As a result, although substrate-supported ZIF-based composites significantly improve material handling and recyclability, many reported systems still face challenges related to mechanical abrasion, surface fouling, or structural degradation during repeated use. In particular, the simultaneous optimization of hierarchical porosity, surface roughness, and mechanical stability remains difficult, often resulting in materials that excel in either sorption performance or durability, but rarely in both [54].

To address these limitations, indirect synthesis of ZIFs using metal oxide- and hydroxide-based nanostructures as self-sacrificing templates has emerged as a promising alternative [55]. This method enables better structural control and facilitates the formation of hierarchically structured materials with abundant exposed active sites and a high specific surface area [56], enhancing their potential for oil/water separation. From a materials design perspective, hierarchically structured ZIF-based composites offer a promising pathway to alleviate the intrinsic trade-offs commonly encountered in conventional porous sorbents. By integrating multiple length scales of porosity within a single architecture, such materials can combine molecular-level selectivity associated with micropores with enhanced mass transport enabled by larger meso- or macropores. In addition, the hierarchical organization of ZIF nanocrystals on mechanically robust scaffolds may improve adsorption kinetics, reduce surface clogging during sorption, and enhance the mechanical durability of the composite system [57]. Despite these advantages, the rational design and controlled synthesis of hierarchically structured ZIF-based sorbents for oil/water separation remain relatively underexplored.

To date, hierarchically structured ZIF-based sorbents have received limited attention in oil/water separation studies. Additionally, studies on ZIF-67-based composites for oil/water separation remain scarce compared to the extensively investigated ZIF-8 [36]. More importantly, the rational integration of hierarchical architecture with mechanical robustness and controlled surface wettability in ZIF-67-based composite sorbents remains insufficiently addressed, despite its critical importance for balancing sorption efficiency, selectivity, and durability in practical oil/water separation systems. Hence, in this study, we demonstrate the synthesis of ZIF-67 from cobalt hydroxide nanosheet arrays as a self-sacrificing template, enabling the formation of a hierarchically structured porous network. To optimize the synthesis process, we employ a microwave-assisted approach, which offers rapid crystallization, improved morphology control, and energy efficiency compared to conventional solvothermal methods [58,59]. The resulting ZIF-67-based composite is systematically evaluated in terms of structural properties, wettability, and oil/water separation efficiency, providing new insights into the potential of hierarchically structured ZIF-based composites for environmental remediation applications.

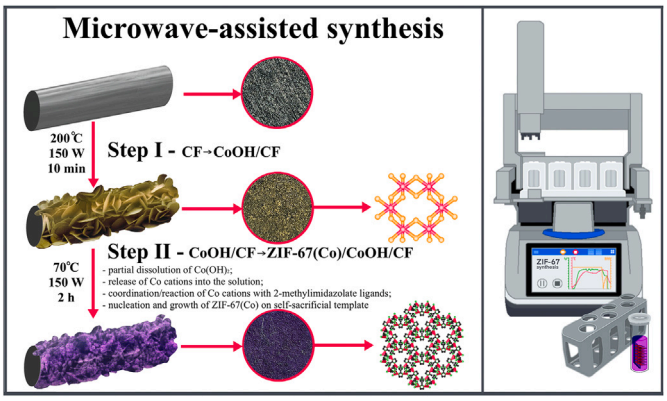

Fig. 1. Schematic representation of the two-step microwave-assisted synthesis route for the ZIF−67 (Co)/CoOH/CF composite sorbent, illustrating the formation of CoOH nanosheet arrays on carbon fibers followed by the growth of ZIF-67 nanocrystals.

2. Materials and methods

2.1. Materials

All chemical reagents used in the experimental work were acquired from Sigma-Aldrich (USA) and Thermo Fisher Scientific (USA). All chemicals were of high purity (analytical or reagent grade), conforming to standards appropriate for synthetic and analytical laboratory procedures. Distilled deionized water was obtained from LUT University's in-house purification system and used in all synthesis and washing steps. Toray carbon fiber paper (TGP-H-060), treated with polytetrafluoroethylene (PTFE), was purchased from Fuel Cell Store (USA).

2.2. Sorbent fabrication

The sorbent synthesis procedure is outlined in Fig. 1. In this study, carbon fibers (CF) were selected as the substrate for active layer deposition due to their comparatively high mechanical strength, chemical stability, and high surface area. Prior to deposition, the CF substrates underwent a thorough cleaning sequence involving 10 min of ultrasonic treatment in acetone, 2 M HCl, and absolute ethanol, respectively. After the removal of surface pollutants, the CF substrates were rinsed with deionized water and subsequently dried at room temperature to prepare them for the deposition process.

The first deposition step involved coating the CF substrates with cobalt hydroxide ($Co(OH)_2$) nanosheet arrays (hereafter denoted as CoOH), which served as self-sacrificing templates for the subsequent synthesis of ZIF-67(Co). The precursor solution for the CoOH layer deposition consisted of 0.1 M $Co(NO_3)_2 \cdot 6H_2O$ and 0.05 M urea in methanol. The CF substrates were immersed in the reaction solution and subjected to microwave irradiation at a maximum power of 150 W for 10 min using a microwave reactor (Discover 2.0, CEM Corporation). The reactor was operated with a set temperature of 200 °C, although the actual reaction temperature was lower than the nominal setting. Following the microwave-assisted synthesis, the resulting CoOH/CF samples were rinsed with absolute ethanol and deionized water, and then dried at 70 °C overnight to remove residual solvents.

The second and final synthesis step involved the in situ growth of ZIF-67(Co) on top of CoOH/CF. To achieve this, the as-prepared CoOH/CF samples were transferred to a solution containing 25 ml of H_2O, 2.5 ml of triethylamine (TEA), and 1.5 M 2-methylimidazole. The solution was exposed to microwave radiation at 150 W maximum power and heated at 70 °C for 2 h. After microwave-assisted synthesis, the ZIF−67 (Co)/CoOH/CF samples were rinsed in absolute ethanol and deionized water and dried at 70 °C overnight to remove the absorbed solvents.

2.3. Material characterization

In this work, all samples were characterized using the following methods. A JEOL JSM-7900F field-emission scanning electron microscope (FE-SEM) was used for high-resolution surface imaging and analysis of surface morphology. SEM images were captured at 1 kV and 20 pA probe current using both an in-chamber secondary electron detector and a backscattered electron detector. A Hitachi S-3400N SEM with energy-dispersive X-ray (EDX) spectroscopy was employed to analyze the elemental composition and distribution of the investigated materials. EDX analysis was performed at an accelerating voltage of 20 kV. Transmission electron microscopy (TEM) analysis was carried out using a Hitachi High-Tech HT7700 TEM equipped with a tungsten filament, operated at an accelerating voltage of 100 kV. X-ray diffraction (XRD) analysis was carried out using a Bruker D8 Advance diffractometer with Cu Kα radiation (λ = 1.5406 Å) generated from a sealed copper tube source. Fourier-Transform Infrared Spectroscopy (FT-IR) analysis was conducted on a PerkinElmer Inc. spectrometer equipped with the universal diamond crystal ATR module over the range of 4000–400 cm^{-1}. Thermogravimetric analysis (TGA) was performed on a NETZSCH STA 449C instrument by heating approximately 5.0 ± 0.1 mg of sample from 25 to 1000 °C at 10°/min under a nitrogen flow of 40 mL/min. Micromeritics 3Flex 3500 was utilized to determine Kr and N_2 adsorption isotherms at −196°C. Specific surface area was calculated from the adsorption isotherms using the Brunauer-Emmett-Teller (BET) equation. Pore size distribution was estimated with density functional theory (DFT) using MicroActive v7.00 software. The pores were assumed to be cylindrical and a DFT kernel for pillared clays was used. The surface chemistry and elemental binding states of the samples were analyzed using X-ray photoelectron spectroscopy (XPS, Nexsa, Thermo Scientific, USA). A monochromatic Al Kα X-ray source (hν = 1486.6 eV) was used for excitation and a dual-mode flood gun with electrons and argon ions was utilized for charge compensation. Data acquisition and analysis were performed using Thermo Avantage v6.10 software.

2.4. Sorbent performance evaluation

The water contact angle (WCA) and oil contact angle (OCA) measurements were performed using a KSV contact angle measurement system equipped with a DMK 21AF04 monochrome camera for image capture. Prior to testing, the samples were dried at 60 °C overnight to remove any residual moisture. The sessile drop method was employed to determine the contact angles. For WCA measurements, a 10 µL droplet of deionized water was placed on the sample surface, and the contact angle was recorded within 10 s of droplet deposition using the system's software. Similarly, for OCA measurements, a 10 µL droplet of edible oil was applied, and the contact angle was determined using the same procedure.

The oil/water separation performance of the sorbents, including bare CF, CoOH/CF, and ZIF-67(Co)/CoOH/CF, was evaluated using a range of organic solvents and oils. These included diesel (Shell), gasoline (Neste), edible oil, toluene, hexane, heptane, hydrocarbon oil, ethylene glycol, ethyl acetate, and acetone. Before the sorption experiments, all sorbents were dried at 60 °C under vacuum for 12 h to remove residual moisture and subsequently weighed. In a typical experiment, a small piece of sorbent (approximately 1 cm × 1 cm) was immersed in 20 mL of the selected organic liquid for 1 min at room temperature. After the sorption process, the sample was carefully removed using tweezers, and the sorbent was immediately weighed to minimize the effect of evaporation. The sorption capacity (Q, wt.%) was calculated according to Eq. (1). All sorption experiments were performed in triplicate, with average values reported and standard deviations calculated from the three independent measurements.

$$Q = \frac{w_1 - w_0}{w_0} \times 100\% \quad (1)$$

where w_1 is the weight of the sorbent after sorption, and w_0 is the initial weight of the dry sorbent.

To further evaluate the oil/water separation performance under more realistic conditions, additional experiments were conducted using model oil-in-water emulsions. The emulsions were prepared by adding diesel to deionized water at an oil-to-water volume ratio of 1:100, followed by the addition of a non-ionic surfactant (Span 80, 0.1 wt.%) to stabilize the dispersed oil droplets. For visualization and quantitative analysis, the diesel phase was dyed using a trace amount of an oil-soluble dye (Sudan IV). The mixture was emulsified by vigorous magnetic stirring for 30 min, followed by ultrasonic treatment for 5 min to obtain a stable, milky oil-in-water emulsion. For the separation tests, a piece of the ZIF−67 (Co)/CoOH/CF composite (approximately 1 cm × 1 cm) was immersed in 10 mL of the prepared emulsion and allowed to interact for 30 min at room temperature. After treatment, the sorbent was removed, and the separation performance was first evaluated qualitatively by visual inspection of the emulsion transparency. For quantitative assessment, the treated and untreated emulsions were analyzed by UV–Vis spectroscopy (V–670, Jasco) by monitoring the absorbance at the characteristic absorption wavelength of Sudan IV (approximately 520 nm). The oil removal efficiency was calculated from the relative decrease in absorbance before and after treatment according to Eq. (2). All emulsion separation experiments were performed in triplicate, and the reported values represent the mean ± standard deviation.

$$R = \left(1 - \frac{A_1}{A_0}\right) \times 100\% \tag{2}$$

where A_0 and A_1 are the UV–Vis absorbance values of the emulsion measured at the characteristic wavelength of Sudan IV before and after treatment, respectively.

For the reusability assessment of the developed ZIF-67(Co)/CoOH/CF composite sorbent, ten consecutive oil/water separation cycles were performed using diesel as the representative oil. After each cycle, the used sorbent was soaked in ethanol to remove residual oil, followed by drying at 60 °C for 1 h. The regenerated sorbent was then reused under identical conditions, and its sorption performance was recorded after each cycle. To evaluate the effect of repeated separation–regeneration cycles on surface wettability and fouling resistance, the WCA of the composite was measured after ten cycles. In addition, post-cycling XRD analysis was performed to examine potential structural changes after repeated diesel separation, as discussed in relation to the reusability and anti-fouling performance.

To evaluate the structural and chemical stability of the sorbent, ultrasound-assisted treatments were performed. The samples were sonicated for 30 min in three different media: distilled water, artificial seawater (0.6 M NaCl solution in distilled water), and diesel. After each treatment, the materials were dried and characterized by XRD to investigate potential changes in crystallinity and phase composition. In addition, a boiling water treatment was carried out to simulate harsh thermal conditions. Samples were immersed in boiling water for 30 min, followed by drying and XRD analysis. The combined XRD results were used to assess the overall durability and structural retention of the material under aggressive conditions. Furthermore, the chemical durability of the composite sorbent was evaluated by immersing the samples in aqueous solutions with different pH values (pH 3 and 11) for 30 min at room temperature. The pH values of the solutions were adjusted using dilute HCl or NaOH. After immersion, the samples were thoroughly rinsed with deionized water, dried at 60 °C, and subsequently subjected to WCA measurements and diesel sorption tests to assess the influence of acidic and alkaline environments on hydrophobicity and separation performance.

To further examine the mechanical stability of the composite coating, a tape-peeling test was performed. Carbon tape was applied to the sorbent surface and then removed to simulate mechanical abrasion. The affected areas were subsequently analyzed using a wide-area 3D measurement system (Keyence VR-3000) to produce surface maps and assess potential delamination or surface damage. To provide a quantitative evaluation of abrasion tolerance, the tape-peeling procedure was repeated for $N = 5$ consecutive cycles using fresh tape in each cycle. After the final peeling cycle, the mechanically challenged samples were subjected to a diesel sorption test under the same conditions as the pristine sorbents. The retained sorption capacity was calculated according to Eq. (3).

$$Q_{\text{retained}} = \frac{Q_N}{Q_0} \times 100\% \tag{3}$$

where Q_0 is the initial sorption capacity of the pristine sorbent, and Q_N is the sorption capacity measured after N consecutive tape-peeling cycles.

3. Results and discussion

3.1. Microwave-assisted synthesis of sorbents

Microwave-assisted synthesis offers distinct advantages compared to conventional thermal methods. During microwave irradiation, the electromagnetic field couples directly with solvent molecules, leading to a rapid temperature increase within the reaction medium and localized superheating. This distinctive property minimizes the wall-heating effect typically observed in conventional heating systems [60]. As a result, energy transfer to the reactants is highly efficient, which accelerates reaction kinetics, shortens synthesis times, and favors the formation of uniform nanostructures [61]. For sorbent development in water treatment applications, such nanostructured materials are particularly advantageous, as their enlarged surface area and well-defined morphologies improve adsorption efficiency and mass transfer processes.

In this study, microwave-assisted synthesis was utilized to reduce the reaction time and to promote the formation of well-defined nanostructured morphologies within the hierarchical composite. As the first step in the fabrication sequence, the CF substrate was coated with CoOH nanosheet arrays (Fig. 2(b)). In contrast to the original procedure [56], methanol, whose high dielectric loss factor enables efficient coupling with the microwave field, was employed as the solvent instead of water. This choice was crucial for enabling the synthesis on the fluorine-modified CF substrate with hydrophobic surface properties, as it allowed effective wetting of the substrate and its full immersion into the reaction solution. As a result, the synthesis required only 10 min, representing a remarkable reduction in processing time compared to conventional hydrothermal approaches, where similar nanostructures typically require 12 h at 90 °C in an autoclave [56].

The actual process conditions monitored during the synthesis of CoOH/CF are presented in Fig. 3(a). The reaction temperature rapidly increased and stabilized at approximately 170 °C (i.e., well above the atmospheric boiling point of methanol), which is possible due to autogenous pressure in the sealed microwave reactor. This elevated temperature was not externally imposed but resulted from efficient

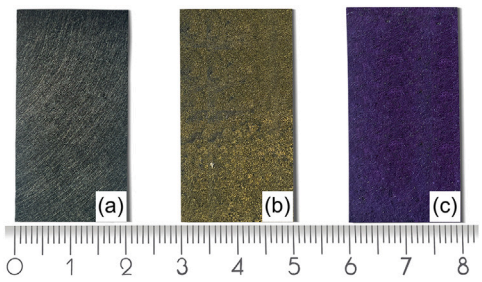

Fig. 2. Photos of sorbent surface changes: (a) bare CF, (b) CoOH/CF, and (c) ZIF-67(Co)/CoOH/CF during the step-by-step preparation of the hierarchically structured composite.

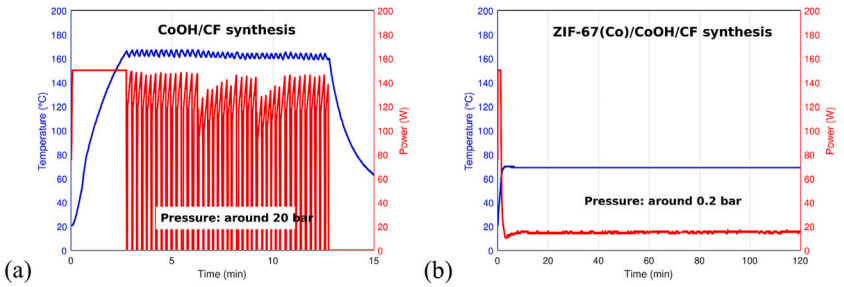

Fig. 3. Process monitoring: time-dependent changes of temperature and power during microwave-assisted synthesis of (a) CoOH/CF and (b) ZIF−67 (Co)/CoOH/CF.

volumetric microwave heating of the methanolic reaction medium, with the temperature effectively constrained by the reactor pressure safety limit (20 bar). Meanwhile, the applied microwave power exhibited a pulsed profile, fluctuating between 0 and 150 W over short intervals to keep the pressure within the safety limit and thus maintain a quasi-steady reaction temperature. Such dynamic regulation of the microwave field is expected to influence nucleation and growth dynamics: the alternating high-power bursts may promote rapid nucleation events, while the intermittent low-power periods allow for controlled crystal growth, ultimately resulting in nanosheet arrays with uniform morphology. Compared to conventional hydrothermal synthesis, this combination of rapid volumetric heating and pulsed microwave input provides a distinct reaction environment that accelerates crystallization without sacrificing structural order [62].

The final synthesis step was the microwave-assisted growth of ZIF−67 (Co) on top of the CoOH nanosheet arrays. The successful synthesis of ZIF−67 (Co)/CoOH/CF was confirmed by a distinct color change of the sample to violet, as shown in Fig. 2(c). A temperature-controlled microwave protocol was employed in this case (Fig. 3(b)). It should be noted that the pulsed microwave power profile was primarily employed during the formation of CoOH nanosheet arrays, where regulation of nucleation and anisotropic growth is critical for achieving uniform sheet-like morphologies and establishing a hierarchical scaffold. In contrast, during the subsequent growth of ZIF−67 (Co) on the pre-formed CoOH template, a quasi-continuous microwave heating mode was sufficient to promote controlled interfacial conversion and crystal growth without requiring additional nucleation control. The reaction temperature was maintained at 70 °C, with an initial power input of 150 W used to rapidly reach the target temperature, followed by near-steady operation at approximately 20 W under a slight overpressure of ~0.2 bar. The total synthesis time was 2 h, representing a substantial reduction compared to conventional synthesis methods of ZIF−67 (Co) reported in the literature [44,46,63]. Accordingly, the obtained material exhibited well-defined ZIF−67 crystallites with sizes in the range of 50–150 nm, as confirmed by SEM and TEM analyses. Such structural features, combining nanoscale crystallites with accessible porosity, make the developed hierarchical ZIF−67 (Co)/CoOH/CF composite highly promising for sorption applications.

Based on the experimental observations, the conversion of the CoOH nanosheet arrays into the ZIF−67 (Co) coating is proposed to occur via an interfacial, solution-mediated transformation. Under the reaction conditions, 2-methylimidazole can coordinate with cobalt species at/near the CoOH surface, while partial near-surface dissolution of CoOH may locally release Co^{2+} ions into the surrounding solution. These cobalt species subsequently react with imidazolate ligands, leading to nucleation and growth of ZIF−67 crystallites preferentially at the CoOH template interface. In addition, triethylamine (TEA) serves as a mild base, facilitating the deprotonation of 2-methylimidazole and thereby promoting coordination and nucleation at the CoOH interface, particularly under microwave-assisted conditions. Such an interfacial dissolution–coordination–recrystallization pathway is consistent with the role of CoOH as a self-sacrificial template and explains the formation of a conformal ZIF−67 layer while largely preserving the hierarchical morphology of the nanosheet scaffold.

Overall, the developed microwave-assisted, template-based fabrication sequence was selected to directly address key limitations commonly associated with conventional ZIF growth methods, including uneven coating, particle agglomeration, weak adhesion, slow kinetics, and limited control over coating morphology/thickness. Specifically, rapid and efficient energy transfer under microwave irradiation accelerates crystallization kinetics and substantially shortens synthesis times, thereby mitigating slow growth and improving process reproducibility. At the same time, the pre-formed CoOH nanosheet arrays serve as a structured intermediate layer that promotes more homogeneous nucleation and continuous coverage during the subsequent ZIF−67 growth step, which helps to alleviate uneven coating formation and reduce the tendency toward particle agglomeration. In addition, growth on the CoOH template strengthens interfacial integration between the ZIF layer and the CF substrate and enables improved control over the resulting surface morphology and effective coating thickness within a scalable processing time window. Together, these features provide a straightforward processing route to obtain a well-adhered and morphologically uniform ZIF−67 (Co)/CoOH/CF composite suitable for sorption-based oil/water separation.

From an environmental and process-efficiency perspective, both stages of the microwave-assisted synthesis route offer advantages compared to conventional hydrothermal or solvothermal approaches. During the formation of CoOH nanosheet arrays, rapid volumetric heating under microwave irradiation accelerates urea decomposition and hydroxide formation, enabling the synthesis to be completed within minutes rather than hours and thereby reducing overall energy input. Similarly, the subsequent microwave-assisted growth of ZIF−67 (Co) proceeds under relatively mild conditions (70 °C, low pressure) with a total reaction time of 2 h, which is substantially shorter than that typically required for solvothermal ZIF-67 synthesis. In addition, direct growth of the ZIF layer on the substrate eliminates the need for post-synthesis powder processing steps, such as filtration or re-dispersion, further simplifying the process. While a comprehensive life-cycle assessment is beyond the scope of this study, the reduced reaction times, moderate operating conditions, and simplified processing suggest that the proposed microwave-assisted route may offer improved time- and energy-efficiency for the preparation of hierarchical ZIF-based sorbents.

3.2. Physical characterization of sorbents

The surface morphology of the synthesized materials was investigated using SEM and TEM as illustrated in Fig. 4. Following the detailed synthesis procedure outlined in Section 2.2, the CF substrate (Fig. 4(a)) was initially coated with CoOH (Fig. 4(b)). The SEM and TEM images reveal that the surface morphology of the as-prepared CoOH/CF is composed of nanosheet arrays with excellent alignment, vertical growth, and a high surface-to-volume ratio. The CoOH/CF coating served a dual role:

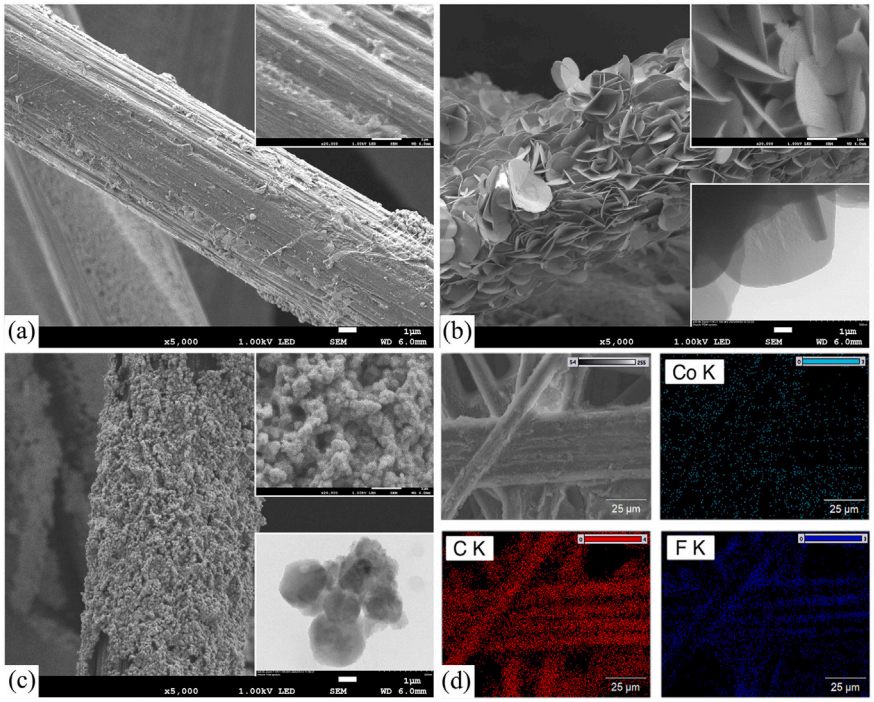

Fig. 4. SEM images of (a) bare CF, (b) CoOH/CF, and (c) ZIF-67(Co)/CoOH/CF. Insets in (a–c) show corresponding high-magnification SEM and TEM images (where applicable). (d) EDX elemental mapping of the ZIF-67(Co)/CoOH/CF composite.

firstly, as self-sacrificial precursors and sources of Co ions, and secondly, as a structural framework for the formation of ZIF-67(Co)/CoOH/CF (Fig. 4(c)). According to the low- and high-magnification SEM and TEM images, the surface of ZIF-67(Co)/CoOH/CF is highly rich in macroporosity, consisting of rhombic dodecahedral-shaped particles homogeneously distributed throughout the fiber surface.

The EDX spectra of bare CF, as-prepared CoOH/CF, and ZIF-67(Co)/CoOH/CF composites are shown in Fig. 5(a). A stepwise emergence of distinctive Co, O, and N peaks can be clearly observed, indicating the successful step-by-step surface modification of CF. Quantitative EDX analysis was performed to evaluate the weight percentage changes of the respective elements at each synthesis step, with the summarized results provided in Table 1. As shown in Table 1, the Co content progressively increases during the modification process, demonstrating the successful deposition of Co species. The EDX elemental mapping results, presented in Fig. 4(d), further confirm a uniform distribution of Co throughout the CF surface. Although a decrease in F content is observed, suggesting that the initial F groups on bare CF are partially replaced or covered during surface functionalization, the remaining amount of approximately 4.5% helps to enhance the hydrophobic properties of the resulting ZIF-67(Co)/CoOH/CF composite (Fig. 7(c)).

The XRD analysis aimed to evaluate the crystallinity of the prepared samples and confirm the presence of the desired structures. As shown in Fig. 5(b), strong diffraction peaks observed in all investigated samples at around 26.39° and 54.37° correspond to the (002) and (004) planes of the graphitic structure in the CF substrate (PDF 00-041-1487) [64]. Additional peaks at 18.09°, 31.56°, and 36.58°, indexed to the (100), (110), and (200) planes, are attributed to the PTFE treatment of the CF substrate (PDF 00-060-1504) [65]. Two further reflections observed at 34.37° and 48.12° match well with polyoxyethylene (PDF 00-064-1486). The presence of these peaks may result from residual polyethylene glycol (PEG)-based compounds used during the surface modification of the fibers. PEG is sometimes employed as a dispersant, surfactant, or binder in PTFE coating formulations to facilitate uniform film deposition on hydrophobic substrates such as CF. The XRD pattern of the synthesized CoOH/CF material exhibited two characteristic peaks located at 2θ = 10.29° and 20.47°, which can be assigned to the (003) and (006) planes of α-CoOH. These peaks are slightly shifted compared to the reference values reported in JCPDS No. 46-0605, where the corresponding reflections are observed at approximately 9.6° and 19.3° [66]. Such deviations may be attributed to variations in the interlayer spacing, potentially caused by the incorporation of guest species, residual solvents, or structural distortions introduced during the synthesis process. The XRD pattern of the synthesized ZIF-67(Co)/CoOH/CF displayed characteristic peaks at 2θ values of 7.51°, 10.53°, 12.89°, 14.87°, 16.63°, 18.21°, 26.69°, 29.82°, 31.61°, and 32.5°, which correspond to the (011), (002), (112), (022), (013), (222), (134), (044), (244), and (235) planes, respectively, in good agreement with the standard data for ZIF-67 (JCPDS No. 43–0144) [63].

The bonding and chemical information of the investigated sorbents were analyzed using FT-IR spectroscopy, as illustrated in Fig. 5(c). The FT-IR spectrum of the PTFE-treated CF displays characteristic absorption bands of CF_2 functional groups. Strong peaks at 1202 cm^{-1} and 1148 cm^{-1} are attributed to the symmetric and asymmetric stretching vibrations of C–F bonds, while additional features at 638, 553, and 499 cm^{-1} correspond to CF_2 rocking, deformation, and wagging modes, respectively [67]. However, in the present spectrum, the CF-related peaks appear weak or absent, which can be attributed to the thickness or high uniformity of the PTFE layer and the inherently low IR activity of graphitic carbon. The FT-IR spectrum of the CoOH/CF composite confirms the successful deposition of the cobalt hydroxide layer, as evidenced by a distinct band near 553 cm^{-1} corresponding to Co–OH bending vibrations [68]. The broad absorption at 3445 cm^{-1} is attributed to the O–H stretching of interlayer water molecules, while the weak peak at 1628 cm^{-1} corresponds to H–O–H bending. The bands at 2924 cm^{-1} and 2823 cm^{-1} are assigned to C–H stretching vibrations of residual alkyl chains (e.g., from alkylamine species) [69]. A peak near 1380 cm^{-1} indicates the presence of interlayer nitrate anions. Additional peaks at 1530, 1035, 825, 742, and 694 cm^{-1} correspond to the vibrational modes of carbonate- and carboxylate-related species—$\nu_{as}(COO^-)/\nu_3(CO_3^{2-})$, $\nu(C-O)/\nu_1(CO_3^{2-})$, $\delta(CO_3^{2-})$, $\delta(COO^-)$, and $\rho(COO^-)$, respectively—supporting the

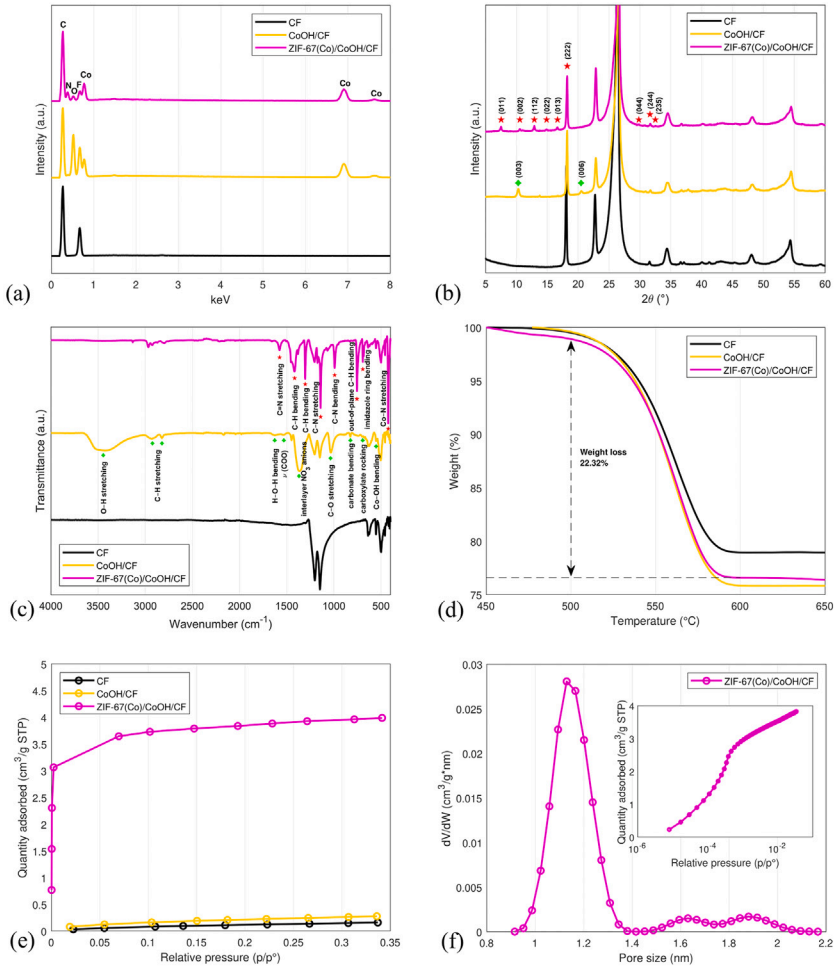

Fig. 5. Physical characterization of the investigated sorbents: (a) EDX spectra, (b) XRD patterns, (c) FT-IR spectra, (d) TGA curves, (e) Kr adsorption isotherms, and (f) pore size distribution of the resulting ZIF-67(Co)/CoOH/CF composite calculated from N_2 adsorption isotherm (inset).

presence of multiple oxygenated coordination environments [68,69]. The FT-IR spectrum of the ZIF-67(Co)/CoOH/CF composite further confirms the successful formation of the ZIF-67 framework. A strong absorption band at 424 cm^{-1} is attributed to the Co–N stretching vibration, indicative of coordination between cobalt ions and nitrogen atoms in 2-methylimidazole ligands. The bending vibration of the imidazole ring is observed at 693 cm^{-1}, while the band at 755 cm^{-1} is assigned to out-of-plane C–H bending vibrations of the imidazole ring, and the band at 1576 cm^{-1} corresponds to ring stretching vibrations (predominantly C=N/C=C) in the 2-methylimidazole framework. Additional signals at 992 cm^{-1} and 1141 cm^{-1} are associated with in-plane ring vibrations with contributions from C–N modes (often reported as a mixed ring/C–N vibration) and C–N stretching vibrations, respectively. Furthermore, in-plane bending vibrations of C–H groups are observed at 1416 cm^{-1} and 1304 cm^{-1}, consistent with previously reported data [70].

The thermal stability of the samples was evaluated using TGA. As shown in Fig. 5(d), all investigated materials exhibited a notable weight loss in the temperature range of 500–600 °C, which can be attributed to the decomposition of organic moieties and the release of volatile components. In this temperature region, the mass losses were approximately 21% for CF, 24% for CoOH/CF, and 23% for ZIF-67(Co)/CoOH/CF. Beyond 600 °C, no substantial changes were observed, suggesting the completion of the major decomposition processes. The final residual masses at 1000 °C were around 77%, 73%, and 75% for CF, CoOH/CF, and ZIF-67(Co)/CoOH/CF, respectively. These results indicate that the thermal stability of the sorbents follows the order: CF > ZIF-67(Co)/CoOH/CF > CoOH/CF. Since the residual masses at 1000 °C are relatively similar across the samples, it can be concluded that the modification of CF with active layers had only a minor impact on its overall thermal stability.

Table 1
Weight percentages of Co, O, N, C, and F elements in CF, CoOH/CF, and ZIF-67(Co)/CoOH/CF sorbents as determined by quantitative EDX analysis.

Sorbent	Co (%)	O (%)	N (%)	C (%)	F (%)
CF	–	–	–	68.94	31.06
CoOH/CF	19.13	22.48	–	43.13	15.26
ZIF-67(Co)/CoOH/CF	25.51	3.77	9.93	56.33	4.46

The specific surface areas of the samples were derived from the Kr adsorption isotherms shown in Fig. 5(e). The pristine CF exhibits a surface area of approximately 0.68 m^2 g^{-1}, which increases to 1.1 m^2 g^{-1} after the deposition of the CoOH nanosheet layer. Following the growth of the ZIF−67 (Co) framework on the CoOH/CF substrate, the surface area increases substantially to 19.2 m^2 g^{-1}, confirming a significant contribution from the porous ZIF−67 (Co) component. The sample mass was recorded after each synthesis step to estimate the mass fraction of the deposited framework. A mass increase of 1.62 wt.% was measured after the ZIF−67 (Co) growth step, suggesting the formation of a relatively

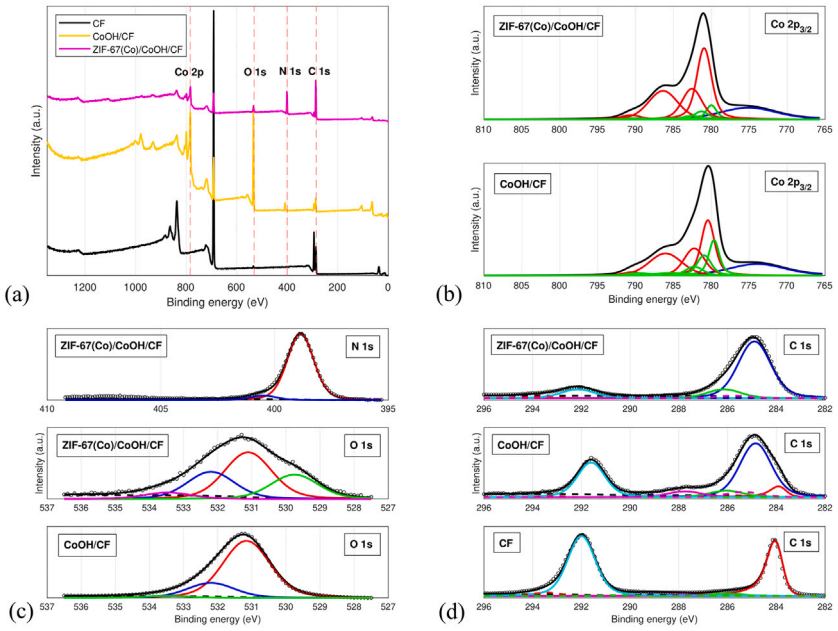

Fig. 6. XPS survey spectrum (a) and high-resolution XPS spectra of the Co $2p_{3/2}$ (b), N 1s and O 1s (c), and C 1s (d) regions for all investigated materials.

Table 2
Atomic concentrations of Co, O, N, C, and F elements in CF, CoOH/CF, and ZIF-67(Co)/CoOH/CF samples as determined from the XPS survey spectra.

Sorbent	Co (%)	O (%)	N (%)	C (%)	F (%)
CF	–	1	–	41	58
CoOH/CF	16	43	6	21	14
ZIF-67(Co)/CoOH/CF	6	5	19	59	11

thin ZIF-based coating distributed over the high-area CF substrate rather than a thick bulk deposit. Based on this mass fraction and the measured composite surface area, the intrinsic surface area of the deposited ZIF−67 (Co) phase was estimated by a mass-balance approach to be on the order of $\sim 10^3$ m^2 g^{-1}. This value should be regarded as an indirect approximation (rather than a directly measured BET surface area), and it is consistent with the range typically reported for ZIF−67 powders in the literature. Analysis of the pore-size distribution (Fig. 5(f)) of the resulting composite indicates predominant microporosity with pore widths in the range of 1–1.4 nm, consistent with the steep uptake at low relative pressures observed in the N_2 adsorption isotherm.

The oxidation states and binding characteristics of the metal ions in the synthesized materials were investigated by XPS analysis (Fig. 6). The binding energy scale of both survey and core-level spectra was calibrated by setting the C–C component of the C 1s spectrum to 284.8 eV. Survey and core-level spectra were acquired using pass energies of 200 eV and 50 eV, respectively. The core-level spectra of C 1s, O 1s, and N 1s were fitted using Voigt peak shapes with an approximate Lorentzian-to-Gaussian ratio of 30:70, and the contribution of inelastically scattered photoelectrons was corrected by Shirley background subtraction. Because the probing depth of XPS is limited to only a few nanometers, it serves as an appropriate technique to confirm the successful deposition and surface composition of the CoOH and ZIF-67(Co) layers (Table 2).

The analysis of the Co 2p core-level spectra in oxides containing mixed-valence Co^{2+} and Co^{3+} species is known to be challenging due to the multiplet splitting characteristic of 3d transition-metal oxides [71] and overlapping Co LMM and O KVV Auger peak structures in spectra collected using Al Kα (hν = 1486.7 eV) radiation [72,73]. The normalized Co $2p_{3/2}$ spectra for the CoOH and ZIF-67(Co) samples reveal a clear difference in the 786–788 eV binding energy region (Fig. 6(b)). To interpret this difference, the Co $2p_{3/2}$ peaks were fitted using the cobalt(II) hydroxide and spinel cobalt oxide multiplet structures proposed by Biesinger *et al.* [71]. In this work, the mixed valence states of Co in the CoOH/CF and ZIF-67(Co)/CoOH/CF samples were estimated based on this multiplet fitting approach, where the cobalt(II) hydroxide components represent Co^{2+} species, while the spinel cobalt oxide components correspond to a combination of Co^{2+} and Co^{3+} oxidation states. The peaks associated with cobalt(II) hydroxide are labeled in red in Fig. 6(b), whereas those corresponding to spinel cobalt oxide are shown in green. A broad feature at lower binding energies in both spectra is attributed to the Co LMM Auger transition. Based on the fitting results, the Co^{3+}/Co^{2+} ratio is higher for the CoOH/CF sample. Previous studies by Fantin, Yang, and Petitto have shown that an increase in the intensity of the Co $2p_{3/2}$ feature at 785–788 eV can be associated with an elevated Co^{2+} content [72,74,75], which further supports the present findings.

In the C 1s spectrum of the CF sample (Fig. 6(d)), the dominant feature is an asymmetric sp^2 C–C component at 284.0 eV accompanied by a π–π^* shake-up satellite near 291 eV. Evidence of PTFE treatment is observed through the CF_2 component at 292.0 eV and the C–CF contribution at 286.3 eV. A weak feature at ~294 eV is assigned to CF_3 (or the high-energy tail of the π–π^* shake-up) [76], while a component at 288.0 eV is attributed to C=O. Upon CoOH deposition (CoOH/CF), the Co atomic concentration increases from 0 to 16 at.% (Table 2), and the C 1s envelope changes accordingly (Fig. 6(d)). The graphitic sp^2 C–C contribution is strongly attenuated, and the CF_2 intensity decreases by approximately one half. New contributions assigned to C–C/C–H (284.8 eV), C–O (285.5 eV), C–N (286.4 eV), and C=O (288.0 eV) become apparent, consistent with the formation of hydroxylated and cobalt-containing surface species. These assignments are consistent with the FTIR results.

The growth of ZIF-67(Co) on top of CoOH/CF is supported by the decreased atomic concentrations of Co and O, together with increased N and C contents on the surface of the ZIF-67(Co)/CoOH/CF sample (Table 2). The N 1s spectrum of ZIF-67(Co)/CoOH/CF shows an intense pyridinic-N signal at 398.8 eV and a weaker component at 400.5 eV

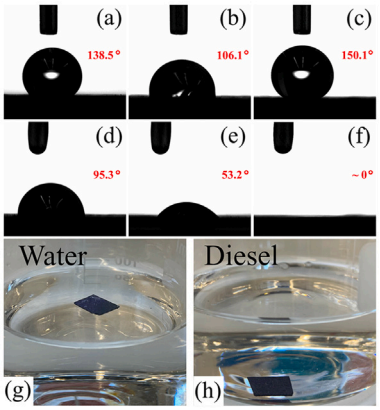

Fig. 7. Contact angle analysis: WCA (a–c) and OCA (d–f) of bare CF, CoOH/CF, and ZIF-67(Co)/CoOH/CF, respectively; digital photographs showing floating on water (g) and sinking in diesel (h) for ZIF-67(Co)/CoOH/CF composite.

attributed to C–N/C–O bonds, whereas the pyridinic-N contribution is not clearly resolved in the N 1s spectrum of CoOH/CF [77]. The O 1s spectrum of CoOH/CF consists of a C=O feature at 531.1 eV and a Co–OH component at 532.2 eV. In addition to these components, the O 1s spectrum of ZIF-67(Co)/CoOH/CF exhibits an intense feature at 529.8 eV corresponding to Co–O bonds [75,78], and a higher-binding-energy structure at 533.5 eV that can be assigned to O–N species. The F 1s peak at 689.0 eV, characteristic of PTFE [76], shows no significant change between the samples, but its reduced intensity supports the step-by-step deposition of CoOH and ZIF-67(Co) on the CF substrate.

3.3. Comparative analysis of sorbent efficiency

WCA and OCA measurements are crucial for evaluating the surface wettability of sorbents, which directly influence their efficiency in selective oil/water separation [30,45]. Materials exhibiting high WCA (> 90°) and low OCA (< 30°) are typically considered hydrophobic and oleophilic, respectively—desirable properties for efficient sorbents. Based on the WCA and OCA measurements, shown in Fig. 7, the fluorine-treated CF substrate exhibited a WCA of 138.5°, indicating strong hydrophobicity, and reduced oil affinity with an OCA of 95.3°. After CoOH layer deposition, the CoOH/CF composite showed a slightly reduced WCA of 106.1°, likely due to the introduction of surface hydroxyl groups that increase surface polarity, and slightly increased oil affinity with an OCA of 53.2°. Despite the improvements observed after CoOH modification, the combination of high hydrophobicity and strong oleophilicity — critical for an ideal sorbent — was not fully achieved at this stage. In contrast, the ZIF-67(Co)/CoOH/CF composite demonstrated a significantly enhanced WCA of 150.1°, indicative of superhydrophobic behavior, along with complete oil spreading (OCA = 0°), confirming its superoleophilic nature. The enhanced superhydrophobicity of ZIF-67(Co)/CoOH/CF can be attributed to the hierarchical micro/nanostructure formed by ZIF-67 crystals, which increases surface roughness and promotes the Cassie–Baxter wetting state. In this state, air pockets trapped beneath water droplets reduce the solid–liquid contact area, resulting in WCA exceeding 150°. Simultaneously, the oleophilic chemical composition and roughness facilitate oil spreading, leading to an OCA of nearly zero, which is critical for selective oil sorption. This selective wetting behavior was further confirmed visually: the ZIF-67(Co)/CoOH/CF composite floated on the water surface while immediately sinking in diesel (Fig. 7(g) and (h)), clearly demonstrating its superhydrophobic and superoleophilic nature.

In the present study, oil/water separation performance is assessed based on sorption capacity, which serves as the primary quantitative metric for separation efficiency in sorbent-based systems. This approach is particularly suitable for evaluating cyclic separation behavior, as it directly reflects the effective uptake and retention of organic liquids during repeated use. The sorption capacity of bare CF, CoOH/CF, and ZIF−67 (Co)/CoOH/CF was evaluated using various organic liquids, as shown in Fig. 8(a). A progressive enhancement in sorption performance was observed across the composite series, highlighting the contribution of each surface modification stage. Compared to bare CF, the CoOH/CF composite exhibited higher sorption capacities for several polar and moderately polar sorbates, including toluene (110 wt.%), ethyl acetate (115 wt.%), and ethylene glycol (152 wt.%), presumably due to favorable dipole–dipole interactions and increased affinity toward hydroxyl-rich surfaces. This trend was further amplified upon the incorporation of ZIF-67 nanocrystals, resulting in substantial improvement across all tested liquids. The final ZIF−67 (Co)/CoOH/CF composite exhibited sorption capacities ranging from 84 to 321 wt.%, with the highest uptakes observed for hydrocarbon oil (321 wt.%), edible oil (252 wt.%), and diesel (164 wt.%).

Table 3
Comparison of WCA/OCA and sorption capacities of various MOF-based composite sorbents for the selective separation of different organic solvents and oils from water.

Sorbent	WCA/OCA	Q (wt.%)	Ref.
ZIF-67(Co)/CoOH/CF	151°/0°	84–321	this work
ZIF-8(Zn)/PES beads	115°/–	15–40	[80]
ZIF-8(Zn)/CNF	135°/–	36–58	[82]
ZIF-8(Zn)/tea bag	142°/0°	70–250	[79]
ZIF-8(Zn)/HFGO	162°/0°	20–280	[42]
MIL-101(Fe)/FG	146°/0°	440–560	[81]
ZIF-8(Zn)/HFGO/Sponge	162°/0°	150–600	[42]
ZIF-8(Zn)/Carbon fabric	150°/0°	1500–2400	[48]
ZIF-8(Zn)/Sponge	140°/0°	1000–3800	[43]
ZIF-67(Co)/PLA aerogel	132°/0°	1500–3000	[46]
ZIF-67(Co)/Sponge	142°/0°	7900–17700	[44]

To contextualize these findings, the performance of the developed composite was compared with other recently reported MOF-based materials, as summarized in Table 3. Although the sorption capacity range of ZIF−67 (Co)/CoOH/CF appears moderate compared to the highest reported values, direct comparison is not always appropriate due to differences in substrate architecture, material density, and testing protocols. Specifically, the composite outperforms pure ZIFs [43,79] and ZIF/polyether sulfone (PES) hybrids [80], and performs comparably to more advanced MOF systems integrated with fluorinated graphene (FG) or highly fluorinated graphene oxide (HFGO) [42,81]. On the other hand, much higher sorption values (up to 17,700 wt.%) reported for sponge- and aerogel-supported composites [44,46] are largely attributed to their ultralow bulk density and highly open macrostructure. For example, melamine sponges typically exhibit bulk densities below 10 mg/cm^3, while carbon fibers are much denser (1700–2000 mg/cm^3), i.e., more than two orders of magnitude higher in bulk density. This contrast significantly influences gravimetric normalization, inflating wt.% values for lightweight substrates.

Moreover, in such sponge-based systems, a considerable portion of the absorbed liquid is likely retained in inter-fiber voids or capillary spaces rather than being confined within the actual material matrix. As a result, the mass of the sponge after sorption increases substantially, even if the intrinsic sorption capacity of the material itself is not dramatically higher. Importantly, gravimetric sorption capacity alone does not fully capture practical performance requirements for oil/water separation sorbents. In contrast to highly compressible sponge- and aerogel-based supports, the CF substrate provides substantially higher mechanical strength and morphological stability, which are critical for handling, regeneration, and repeated separation cycles. The rigid and robust CF framework helps preserve the composite architecture and the active surface morphology during use, thereby supporting more reliable performance in practical scenarios where mechanical deformation, abrasion,

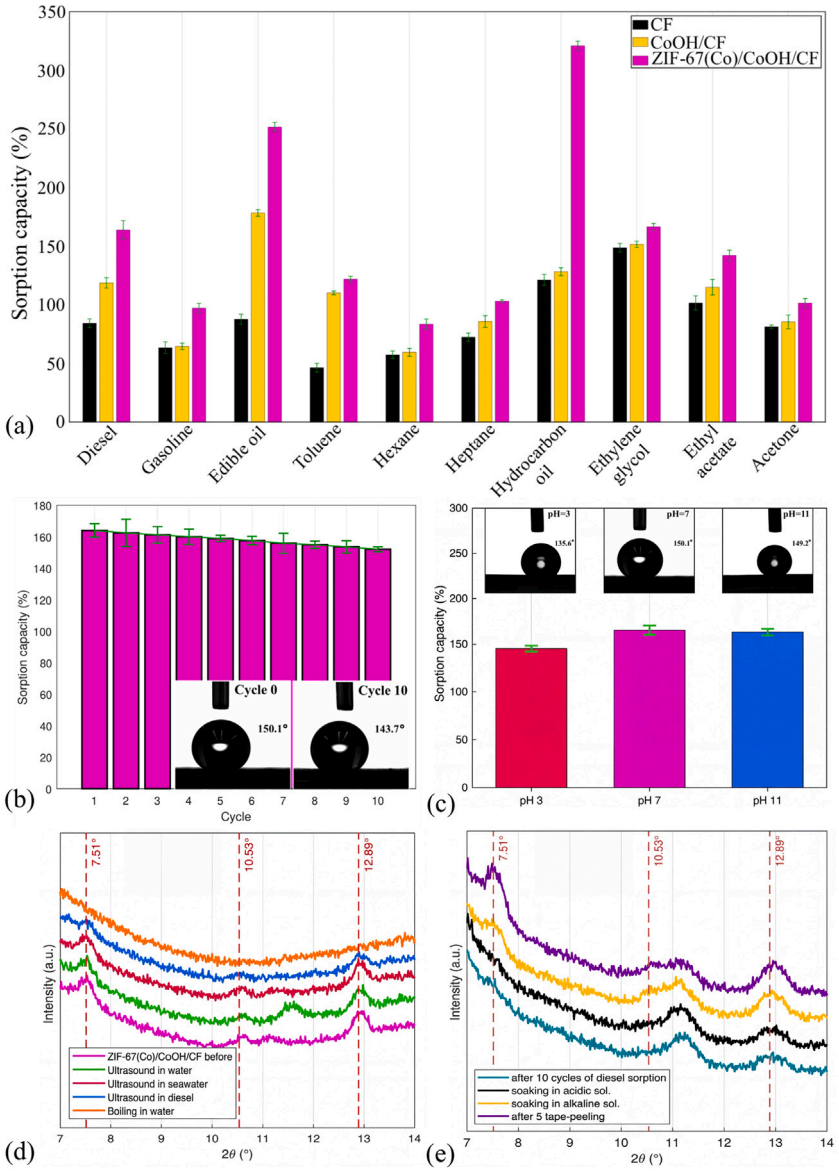

Fig. 8. (a) Sorption capacities of bare CF, CoOH/CF, and ZIF-67(Co)/CoOH/CF toward various organic sorbates. (b) Reusability of ZIF-67(Co)/CoOH/CF over ten consecutive diesel separation cycles (inset: WCA images of the pristine sample and after 10 cycles). (c) Diesel sorption capacity and corresponding WCA of ZIF-67(Co)/CoOH/CF after 30 min exposure to acidic (pH 3) and alkaline (pH 11) aqueous solutions. Data are presented as the mean of three independent measurements ($n = 3$); the green error bars represent the standard deviation. (d,e) XRD patterns of the composite after the stability tests.

and long-term durability are key concerns. Therefore, while ultralight sponges may exhibit exceptionally high wt.% values, CF-supported composites offer a more mechanically resilient and application-relevant platform for stable and reusable oil/water separation.

To further rationalize the enhanced sorption performance of the ZIF−67 (Co)/CoOH/CF composite, it is useful to consider the synergistic role of its hierarchical structure, which presumably contributes beyond the effects of superhydrophobicity and overall surface area alone. At the nanoscale, the intrinsic microporosity of ZIF-67 provides abundant adsorption sites and promotes affinity toward organic molecules, supporting effective uptake and retention. At larger length scales, the structural organization formed by ZIF-67 nanocrystals grown on CoOH nanosheet arrays (whose characteristic dimensions exceed those of the ZIF crystallites) is expected to generate an open, interconnected network with interparticle voids and short diffusion pathways. Such a configuration can facilitate rapid wetting and penetration of organic liquids into the composite and reduce mass-transfer limitations compared to densely packed or powder-like ZIF structures. In addition, the porous carbon fiber framework provides continuous transport channels and mechanical support, enabling efficient liquid access to active regions while maintaining structural integrity during handling and repeated use. Overall, the hierarchical integration of adsorption sites with interconnected transport pathways is therefore believed to promote fast capture and efficient distribution of organic liquids throughout the composite, helping to mitigate surface clogging and sustain high separation efficiency under practical conditions.

To evaluate the separation performance under more realistic conditions, the ZIF−67 (Co)/CoOH/CF composite was further tested using a surfactant-stabilized oil-in-water emulsion (diesel in water, 1:100 v/v, Span 80), where the diesel phase was dyed with Sudan IV for UV–Vis quantification. As shown in Fig. 9(a), the emulsion became visibly more transparent after treatment, indicating effective removal of dispersed oil droplets. This observation is supported by UV–Vis measurements at ~520 nm: the absorbance decreased from $A_0 = 0.529 \pm 0.008$ (untreated

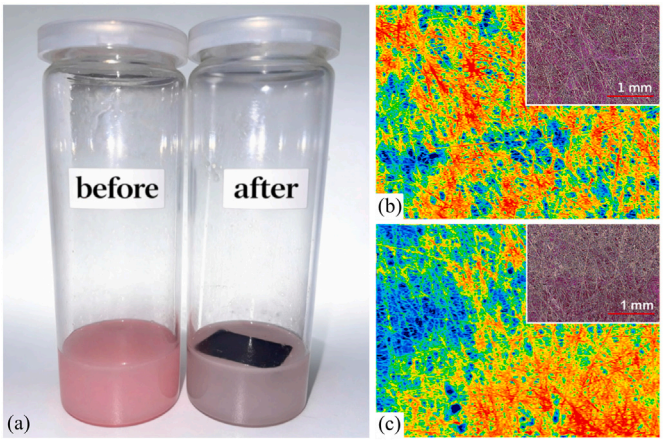

Fig. 9. (a) Photographs of a diesel-in-water emulsion (diesel:water = 1:100 v/v, 0.1 wt.% Span 80; dyed with Sudan IV) before and after treatment with ZIF–67 (Co)/CoOH/CF. (b,c) Wide-area 3D surface maps of the composite before and after a carbon tape-peeling test, respectively, highlighting abrasion-induced changes of the outermost coating layer.

emulsion) to $A_1 = 0.128 \pm 0.005$ after 30 min of contact (mean ± SD, $n = 3$), corresponding to an oil removal efficiency of 75.8 ± 0.7% (Eq. 2). Given the increased separation difficulty associated with surfactant-stabilized microdroplets, these results are presented as a proof-of-concept demonstrating that the composite remains effective beyond simple immiscible oil/water systems.

The long-term reusability and stability of the ZIF–67 (Co)/CoOH/CF composite were systematically evaluated for practical applications. As shown in Fig. 8(b), the ZIF–67 (Co)/CoOH/CF composite retained over 92% of its initial sorption capacity after ten consecutive diesel separation cycles, demonstrating excellent reusability. To assess the effect of repeated oil/water separation on surface wettability, the water contact angle (WCA) was measured after ten separation–regeneration cycles. The WCA decreased only slightly from 150.1° for the pristine sample to 143.7° after ten cycles, indicating that the superhydrophobic surface characteristics were largely preserved (Fig. 8(b), inset). In addition, the self-cleaning and anti-fouling performance of the composite was evaluated by post-cycling characterization. The XRD pattern recorded after ten separation–regeneration cycles shows no noticeable changes in peak positions or relative intensities compared with the pristine sample, indicating that the crystalline framework remains intact during repeated operation (Fig. 8(e)). Together with the minor change in WCA and the retained separation/sorption performance, these results support effective solvent-assisted regeneration and good resistance to persistent fouling.

Ultrasound-assisted treatments were performed to assess structural robustness. The XRD analysis, depicted in Fig. 8(d), revealed that the characteristic peaks remained unchanged after sonication in distilled water and artificial seawater, indicating strong crystallinity retention. In contrast, after diesel exposure, a slight decrease in peak intensity was observed, likely due to the sorption of hydrocarbons within the material pores. Boiling water treatment caused pronounced structural degradation, evidenced by a strong suppression (nearly disappearance) of the characteristic XRD reflections of the ZIF-67 phase. This behavior is consistent with partial hydrolysis/amorphization of ZIF-67 under extreme hydrothermal conditions, indicating that boiling water represents a harsh stability limit for the composite.

In addition, the chemical durability of the ZIF–67 (Co)/CoOH/CF composite under different pH conditions was evaluated to assess its stability in acidic and alkaline aqueous environments. After exposure to solutions with pH 3 and 11, the composite maintained high water-repellency, with water contact angles of 135.6° (pH 3) and 149.2° (pH 11) (Fig. 8(c)). Notably, after acidic treatment the characteristic pink surface coloration partially faded, suggesting that the outermost coating layer on the most exposed fibers is more susceptible to acidic conditions. However, owing to the intrinsic hydrophobicity and the multilayer/hierarchical structure of the composite, the inner fiber layers remain largely protected and coated. This is supported by XRD analysis, where a decrease in peak intensities was observed after pH 3 exposure while the characteristic diffraction peaks remained clearly detectable, indicating preserved phase identity. In contrast, alkaline treatment did not produce noticeable changes in the XRD peak intensities, consistent with the minimal change in water contact angle. Consistently, the average diesel sorption capacity remained high after pH exposure, decreasing by only ~ 12% (pH 3) and ~ 1% (pH 11) relative to the neutral reference. Overall, these results demonstrate good chemical durability of the composite: despite the more challenging acidic environment, it retained strong hydrophobicity and high oil uptake, supporting its practical applicability for oil/water separation in water streams with variable pH.

Mechanical robustness of the coating was first assessed using a tape-peeling test, where wide-area 3D surface mapping revealed partial removal of the top layer (Fig. 9(b, c)), highlighting the effect of mechanical abrasion. Notably, increasing the number of tape-peeling rounds to $N = 5$ did not lead to visible macroscopic changes in the sample. This behavior can be rationalized by the nature of the CF substrate and the hierarchical architecture of the composite: the adhesive tape primarily interacts with and partially removes the coating from the most exposed outer carbon fibers, whereas the inner fiber layers remain largely protected and structurally intact. This interpretation is supported by the XRD patterns recorded after the tape-peeling protocol (Fig. 8(e)), which show no detectable loss of the characteristic diffraction features of the active phase, indicating preserved structural integrity. In addition, the functional consequence of repeated abrasion was quantified by measuring the diesel sorption capacity after $N = 5$ cycles, yielding a high retained sorption capacity of 96% relative to the pristine sample (Eq. 3). Taken together, these results demonstrate that the ZIF–67 (Co)/CoOH/CF composite combines high sorption efficiency and selectivity with resilience to mechanical stress, complementing its chemical and thermal stability. Further enhancement of durability and the development of post-treatment strategies could be explored in future studies to optimize long-term performance for practical oil/water separation applications.

4. Conclusions

In this work, a hierarchical ZIF–67 (Co)/CoOH/CF composite was developed via a two-step microwave-assisted strategy, enabling the rapid formation of cobalt hydroxide nanosheet arrays and their subsequent conversion into ZIF-67 nanocrystals. This design resulted in a well-integrated composite architecture that combines nanoscale crystallinity and intrinsic microporosity with a mechanically robust carbon fiber substrate. As a consequence, the surface wettability could be precisely tuned from hydrophobic/oleophilic to superhydrophobic/superoleophilic, which is essential for selective oil/water separation. The resulting composite exhibited high sorption capacities toward a broad range of organic liquids and outperformed many previously reported MOF-based sorbents supported on dense substrates, while maintaining stable performance during repeated separation cycles and under various harsh experimental conditions. Moreover, as a proof of concept, the composite exhibited measurable performance in treating surfactant-stabilized diesel-in-water emulsions. From a broader perspective, this study demonstrates that a rational hierarchical design, together with a rapid microwave-assisted synthesis route based on a self-sacrificing template, provides an effective strategy to address the intrinsic trade-offs between sorption efficiency, selectivity, and mechanical robustness that commonly limit porous oil/water separation materials. Although boiling-water treatment represents a harsh stability limit for the material and partial mechanical abrasion was detected, the overall balance of

efficiency, durability under relevant operating conditions, and reusability highlights the practical potential of the developed composite. Future work will focus on post-treatment and structural optimization strategies to further enhance durability and extend the operational lifetime of hierarchically structured ZIF-based sorbents under demanding operating conditions.

CRediT authorship contribution statement

Georgy Givirovskiy: Writing – original draft, Visualization, Validation, Methodology, Investigation, Formal analysis, Data curation, Conceptualization. **Daria Givirovskaia:** Writing – original draft, Visualization, Validation, Methodology, Investigation, Formal analysis, Conceptualization. **Yerkezhan Yerkinbekova:** Writing – review & editing, Investigation. **Ville Laitinen:** Writing – review & editing, Investigation, Formal analysis. **Liisa Puro:** Writing – review & editing, Investigation, Formal analysis. **Timo Laakso:** Writing – review & editing, Investigation, Formal analysis. **Sari Granroth:** Writing – original draft, Investigation, Formal analysis. **Ermei Mäkilä:** Writing – original draft, Investigation, Formal analysis. **Eveliina Repo:** Writing – review & editing, Supervision, Resources, Project administration, Conceptualization.

Declaration of generative AI and A-assisted technologies in the writing process

During the preparation of this work, the authors used ChatGPT for language polishing. After using this tool, the authors reviewed and edited the content as needed and take full responsibility for the final content of the manuscript.

Declaration of competing interest

The authors declare that they have no known competing financial interests or personal relationships that could have appeared to influence the work reported in this paper.

Acknowledgement

The authors gratefully acknowledge the support of the European Regional Development Fund, ELY Centre for South Savo (project number: A90790), as well as the Research Council of Finland (decision numbers: 330076 and 358148).

Data availability

Data will be made available on request.

References

[1] C. Brussaard, L. Peperzak, S. Beggah, L. Wick, B. Weurz, J. Weber, et al., Immediate Ecotoxicological Effects of Short-Lived Oil Spills on Marine Biota, Nat. Commun. 7 (2016) 1–11.
[2] C. Peterson, S. Rice, J. Short, D. Esler, J. Bodkin, B. Ballachey, et al., Long-Term Ecosystem Response to the Exxon Valdez Oil Spill, Sci. 302 (2004) 2082–2086.
[3] N. Sainjan, C. Saravanakumar, P. Ramachandran, R. Robin, R. Ramachandran, Oil-Spill Triggered Shift in Indigenous Microbial Structure and Functional Dynamics in Different Marine Environmental Matrices, Sci. Rep. 9 (2019) 1354.
[4] O. Hettithanthri, T.B.T. Nguyen, T. Fiedler, C. Phan, M. Vithanage, S. Pallewatta, et al., A review of oil spill dynamics: Statistics, impacts, countermeasures, and weathering behaviors, Asia-Pac. J. Chem. Eng. 19 (2024) e3128.
[5] B. Purohit, S. Tewari, K. Prasad, V.K. Talari, N. Pandey, P. Choudhury, et al., Marine oil spill clean-up: A review on technologies with recent trends and challenges, Reg. Stud. Mar. Sci. 80 (2024) 103876.
[6] A. Dhaka, P. Chattopadhyay, A review on physical remediation techniques for treatment of marine oil spills, J. Exp. Med. 288 (2021) 112428.
[7] Z. Zhu, F. Merlin, M. Yang, K. Lee, B. Chen, B. Liu, et al., Recent advances in chemical and biological degradation of spilled oil: A review of dispersants application in the marine environment, J. Hazard. Mater. 436 (2022) 129260.
[8] A.J. Pete, B. Bharti, M.G. Benton, Nano-enhanced Bioremediation for Oil Spills: A Review, ACS ES&T Eng. 1 (2021) 928–946.
[9] Z. Chu, Y. Feng, S. Seeger, Oil/Water Separation with Selective Superantiwetting/Superwetting Surface Materials, Angew. Chem. Int. Ed. 54 (2015) 2328–2338.
[10] Q. Ma, H. Cheng, A.G. Fane, R. Wang, H. Zhang, Recent Development of Advanced Materials with Special Wettability for Selective Oil/Water Separation, Small 12 (2016) 2186–2202.
[11] S. Gupta, N.-H. Tai, Carbon materials as oil sorbents: a review on the synthesis and performance, J. Mater. Chem. A 4 (2016) 1550–1565.
[12] T.T.N. Vo, D.I. Yu, H.S. Ahn, Tuning Carbon Material Modified Commercial Sponge Toward Pragmatic Oil Spill Cleanup, Adv. Mater. Interfaces 10 (2023) 2300107.
[13] B. Doshi, M. Sillanpää, S. Kalliola, A review of bio-based materials for oil spill treatment, Water Res. 135 (2018) 262–277.
[14] S. Li, L. Huang, D. Wang, S. Zhou, X. Sun, R. Zhao, et al., A review of 3D superhydrophilic porous materials for oil/water separation, Sep. Purif. Technol. 326 (2023) 124847.
[15] Y. Liu, H. Zhang, P. Wang, Z. He, G. Dong, 3D-printed bionic superhydrophobic surface with petal-like microstructures for droplet manipulation, oil-water separation, and drag reduction, Mater. Des. 219 (2022) 110765.
[16] N. Haridharan, D. Sundar, L. Kurrupasamy, S. Anandan, C.-H. Liu, J.J. Wu, Oil spills adsorption and cleanup by polymeric materials: A review, Polym. Adv. Technol. 33 (2022) 1353–1384.
[17] A.T. Hoang, S. Nizetic, X.Q. Duong, L. Rowinski, X.P. Nguyen, Advanced superhydrophobic polymer-based porous absorbents for the treatment of oil-polluted water, Chemosphere 277 (130274) (2021).
[18] H. Bi, C.N. Mulligan, K. Lee, B. Zhang, Z. Chen, C. An, Nanotechnology for oil spill response and cleanup in coastal regions, Environ. Sci. Nano 12 (1) (2025) 41–47, https://doi.org/10.1039/D4EN00954A.
[19] A. Omidi, F. Firoozbakht, H. Zali Boeini, R.S. Varma, Magnetic Hydrophobic Cellulose Nanocomposites for Efficient Removal of Oil Spills and Organic Solvents, Energy Fuels 38 (2024) 23367–23376.
[20] Y. Wu, B.M. Weckhuysen, Separation and Purification of Hydrocarbons with Porous Materials, Angew. Chem, Int. Ed. 60 (2021) 18930–18949.
[21] S. Rasouli, N. Rezaei, H. Hamedi, S. Zendehboudi, X. Duan, Superhydrophobic and superoleophilic membranes for oil-water separation application: A comprehensive review, Mater. Des. 204 (2021) 109599.
[22] Q. Gu, M. Kotobuki, C.H. Kirk, M. He, G.J.H. Lim, T.C.A. Ng, et al., Overcoming the Trade-off between Water Permeation and Mechanical Strength of Ceramic Membrane Supports by Interfacial Engineering, ACS Appl. Mater. Interfaces. 13 (2021) 29199–29211, PMID: 34126737.
[23] W. Chen, Z. Ren, Y. Lin, X. Chen, Interpenetrating metal-polymer frameworks with designed gradient porosity for robust superhydrophobic oil absorbents, J. Environ. Chem. Eng. 14 (2026) 120548.
[24] W. Zhenggong, X. Luo, Z. Song, K. Lu, S. Zhu, Y. Yang, et al., Microporous polymer adsorptive membranes with high processing capacity for molecular separation, Nat. Commun. 13 (2022) 4169.
[25] D. Li, A. Yadav, H. Zhou, K. Roy, P. Thanasekaran, C. Lee, Advances and Applications of Metal-Organic Frameworks (MOFs) in Emerging Technologies: A Comprehensive Review, Glob. Challenges 8 (2024) 2300244.
[26] D. Givirovskaia, G. Givirovskiy, M. Haapakoski, S. Hokkanen, V. Ruuskanen, S. Salo, et al., Modification of face masks with zeolite imidazolate framework-8: A tool for hindering the spread of COVID-19 infection, Microporous Mesoporous Mater. 334 (2022) 111760.
[27] D. Givirovskaia, G. Givirovskiy, V. Laitinen, Y. Park, P. Amin, A. ur Rehman, et al., Efficient water splitting with a MOF-74(Ni)-derived composite electrocatalyst prepared via microwave- and laser-assisted synthesis, Nano Res. 18 (2) (2025) 94907100, https://doi.org/10.26599/NR.2025.94907100.
[28] L. Jiao, J.Y.R. Seow, W.S. Skinner, Z.U. Wang, H.-L. Jiang, Metal-organic frameworks: Structures and functional applications, Mater. Today. 27 (2019) 43–68.
[29] Y. Cui, B. Li, H. He, W. Zhou, B. Chen, G. Qian, Metal-Organic Frameworks as Platforms for Functional Materials, Acc. Chem. Res. 49 (2016) 1–11.
[30] A.M. Abudayyeh, L.A. Mahmoud, V.P. Ting, S. Nayak, Metal-Organic Frameworks (MOFs) and Their Composites for Oil/Water Separation, ACS Omega 9 (2024) 47374–47394.
[31] K. Jayaramulu, F. Geyer, A. Schneemann, Å. Kment, M. Otyepka, R. Zboril, et al., Hydrophobic Metal-Organic Frameworks, Adv. Mater. 31 (2019) 1900820.
[32] M. Shahmirzaee, J. Abdi, A. Hemmati-Sarapardeh, M. Schaffie, M. Ranjbar, A. Khataee, Metal-organic frameworks as advanced sorbents for oil/water separation, J. Mol. Liq. 363 (2022) 119900.
[33] W.-G. Cui, T.-L. Hu, X.-H. Bu, Metal-Organic Framework Materials for the Separation and Purification of Light Hydrocarbons, Adv. Mater. 32 (2020) 1806445.
[34] Y.V. Kaneti, S. Dutta, M.S.A. Hossain, M.J.A. Shiddiky, K.-L. Tung, F.-K. Shieh, et al., Strategies for Improving the Functionality of Zeolitic Imidazolate Frameworks: Tailoring Nanoarchitectures for Functional Applications, Adv. Mater. 29 (2017) 1700213.
[35] K.S. Park, Z. Ni, A.P. Côté, J.Y. Choi, R. Huang, F.J. Uribe-Romo, et al., Exceptional chemical and thermal stability of zeolitic imidazolate frameworks, Proc. Natl. Acad. Sci. 103 (2006) 10186–10191.
[36] M. Shahmirzaee, A. Hemmati-Sarapardeh, M.M. Husein, M. Schaffie, M. Ranjbar, A review on zeolitic imidazolate frameworks use for crude oil spills cleanup, Adv. Geo-Energy Res. 3 (2019) 320–342.
[37] K. Noh, J. Lee, J. Kim, Compositions and Structures of Zeolitic Imidazolate Frameworks, Isr. J. Chem. 58 (2018) 1075–1088.
[38] S. Lee, D. Nam, D.C. Yang, W. Choe, Unveiling Hidden Zeolitic Imidazolate Frameworks Guided by Intuition-Based Geometrical Factors, Small 19 (2023) 2300036.
[39] X. Gong, L. Zhang, Y. Liu, M. Zhu, A review on zeolitic imidazolate framework-8 based materials with special wettability for oil/water separation, J. Environ. Chem. Eng. 11 (2023) 111360.
[40] Q. Ma, G. Li, X. Liu, Z. Wang, Z. Song, H. Wang, Zeolitic imidazolate framework-8 film coated stainless steel meshes for highly efficient oil/water separation, Chem. Commun. 54 (2018) 5530–5533.

[41] X. Gao, Q. Ma, Z. Jin, P. Nian, Z. Wang, Switchable superlyophobic zeolitic imidazolate framework-8 film-coated stainless-steel meshes for selective oil-water emulsion separation with high flux, New J. Chem. 44 (2020) 13534–13541.
[42] K. Jayaramulu, K.K.R. Datta, C. Rösler, M. Petr, M. Otyepka, R. Zboril, et al., Biomimetic Superhydrophobic/Superoleophilic Highly Fluorinated Graphene Oxide and ZIF-8 Composites for Oil-Water Separation, Angew. Chem. Int. Ed. 55 (2016) 1178–1182.
[43] Z. Lei, Y. Deng, C. Wang, Multiphase surface growth of hydrophobic ZIF-8 on melamine sponge for excellent oil/water separation and effective catalysis in a Knoevenagel reaction, J. Mater. Chem. A 6 (2018) 3258–3263.
[44] Y. Zhang, N. Zhang, S. Zhou, X. Lv, C. Yang, W. Chen, et al., Facile Preparation of ZIF-67 Coated Melamine Sponge for Efficient Oil/Water Separation, Ind. Eng. Chem. Res. 58 (2019) 17380–17388.
[45] L. Zhang, J. Xie, X. Luo, X. Gong, M. Zhu, Enhanced hydrophobicity of shell-ligand-exchanged ZIF-8/melamine foam for excellent oil-water separation, Chem. Eng. Sci. 273 (2023) 118663.
[46] W. Qu, Z. Wang, X. Wang, Z. Wang, D. Yu, D. Ji, High-hydrophobic ZIF-67@PLA honeycomb aerogel for efficient oil-water separation, Colloids Surf. A Physicochem. Eng. Aspects. 658 (2023) 130768.
[47] S. Xu, L.-F. Ren, Q. Zhou, H. Bai, J. Li, J. Shao, Facile ZIF-8 functionalized hierarchical micronanofiber membrane for high-efficiency separation of water-in-oil emulsions, J. Appl. Polym. Sci. 135 (2018) 46462.
[48] M. Shahmirzaee, A. Hemmati-Sarapardeh, M.M. Husein, M. Schaffie, M. Ranjbar, Development of a powerful zeolitic imidazolate framework (ZIF-8)/carbon fiber nanocomposite for separation of hydrocarbons and crude oil from wastewater, Microporous Mesoporous Mater. 307 (2020) 110463.
[49] Y. Li, D. Wang, G. Xu, L. Qiao, Y. Li, H. Gong, et al., ZIF-8/PI Nanofibrous Membranes With High-Temperature Resistance for Highly Efficient $PM_{0.3}$ Air Filtration and Oil-Water Separation, Front. Chem. 9 (2021).
[50] W. Liu, L. Yu, X. Cui, C. Tan, M. Zhang, D. Wu, et al., Polyphenylene Sulfide Ultrafine Viscous Fibrous Membrane Modified by ZIF-8 for Highly Effective Oil/Water Separation under High Salt or Alkaline Conditions, Membranes 12 (2022).
[51] E. Barankova, N. Pradeep, K.-V. Peinemann, Zeolite-imidazolate framework (ZIF-8) membrane synthesis on a mixed-matrix substrate, Chem. Commun. 49 (2013) 9419–9421.
[52] X. Feng, M.A. Carreon, Kinetics of transformation on ZIF-67 crystals, J. Cryst. Growth 418 (2015) 158–162.
[53] H. Zhu, Q. Zhang, B.-G. Li, S. Zhu, Engineering Elastic ZIF-8-Sponges for Oil-Water Separation, Adv. Mater. Interfaces 4 (2017) 1700560.
[54] J. Wang, J. Yang, H. Zhu, B.-G. Li, S. Zhu, In-situ construction of hierarchically porous MOF monoliths using high internal phase emulsion templates, Chem. Eng. J. 456 (2023) 141026.
[55] G. Cai, W. Zhang, L. Jiao, S.-H. Yu, H.-L. Jiang, Template-Directed Growth of Well-Aligned MOF Arrays and Derived Self-Supporting Electrodes for Water Splitting, Chem 2 (2017) 791–802.
[56] J. Zhou, Y. Dou, A. Zhou, R.-M. Guo, M.-J. Zhao, J.-R. Li, MOF Template-Directed Fabrication of Hierarchically Structured Electrocatalysts for Efficient Oxygen Evolution Reaction, Adv. Energy Mater. 7 (2017) 1602643.
[57] H. Saini, E. Otyepková, A. Schneemann, R. Zbořil, M. Otyepka, R.A. Fischer, et al., Hierarchical porous metal-organic framework materials for efficient oil-water separation, J. Mater. Chem. A 10 (2022) 2751–2785.
[58] I. Thomas-Hillman, A. Laybourn, C. Dodds, S.W. Kingman, Realising the environmental benefits of metal-organic frameworks: recent advances in microwave synthesis, J. Mater. Chem. A 6 (2018) 11564–11581.
[59] A. Kumar, Y. Kuang, Z. Liang, X. Sun, Microwave chemistry, recent advancements, and eco-friendly microwave-assisted synthesis of nanoarchitectures and their applications: a review, Mater. Today Nano. 11 (2020) 100076.
[60] Y.-J. Zhu, F. Chen, Microwave-Assisted Preparation of Inorganic Nanostructures in Liquid Phase, Chem. Rev. 114 (2014) 6462–6555.
[61] R. Vakili, S. Xu, N. Al-Janabi, P. Gorgojo, S.M. Holmes, X. Fan, Microwave-assisted synthesis of zirconium-based metal organic frameworks (MOFs): Optimization and gas adsorption, Microporous Mesoporous Mater. 260 (2018) 45–53.
[62] N.T.K. Thanh, N. Maclean, S. Mahiddine, Mechanisms of Nucleation and Growth of Nanoparticles in Solution, Chem. Rev. 114 (2014) 7610–7630.
[63] Q. Wang, Z. Yu, X. Zhu, Q. Xiang, H. Chen, Y. Pang, ZIF-67 modified MXene/sepiolite composite membrane for oil-water separation and heavy metal removal, J. Ind. Eng. Chem. 115 (2022) 314–328.
[64] L. Li, Y. Wang, T. Lei, Z. Xie, Y. Liang, Structure and properties of carbon fiber paper with gradient porous structure, J. Porous Mater. 31 (2024) 1–9.
[65] P.R. Riley, P. Joshi, H. Penchev, J. Narayan, R.J. Narayan, One-Step Formation of Reduced Graphene Oxide from Insulating Polymers Induced by Laser Writing Method, Crystals 11 (2021).
[66] B. Cao, C. Luo, J. Lao, H. Chen, R. Qi, H. Lin, et al., Facile Synthesis of 3d Transition-Metal-Doped α-$Co(OH)_2$ Nanomaterials in Water-Methanol Mediated with Ammonia for Oxygen Evolution Reaction, in: ACS Omega, vol. 4, American Chemical Society (ACS), 2019, pp. 16612–16618.
[67] S. Bhullar, A. Celik Bedelogylu, M. Jun, Characterization and Auxetic effect of Polytetrafluoroethylene Tubular structure, Int. J. Adv. Sci. Eng. 1 (2014) 8–13.
[68] F. Zhang, C. Yuan, X. Lu, L. Zhang, Q. Che, X. Zhang, Facile growth of mesoporous Co_3O_4 nanowire arrays on Ni foam for high performance electrochemical capacitors, J. Power Sources 203 (2012) 250–256.
[69] S. Zhou, W. Wei, Y. Zhang, S. Cui, W. Chen, L. Mi, Heterojunction α-$Co(OH)_2$/α-$Ni(OH)_2$ nanorods arrays on Ni foam with high utilization rate and excellent structure stability for high-performance supercapacitor, Sci. Rep. 9 (2019) 1–12.
[70] S. Vadivel, S. Sanjana, M. Anbazhagan, A. Shameem, R.M. Jauhar, S. Babu, Facile synthesis and asymmetric device fabrication of zeolite like Co-MOF as a promising electrode material with improved cyclic stability, J. Mater. Sci.: Mater. Electron. 35 (2024) 1–14.
[71] M. Biesinger, B. Payne, A. Grosvenor, L. Lau, A. Gerson, R. Smart, Resolving surface chemical states in XPS analysis of first row transition metals, oxides and hydroxides: Cr, Mn, Fe, Co and Ni, Appl. Surf. Sci. 257 (2011) 2717–2730.
[72] R. Fantin, A. Van Roekeghem, A. Benayad, Revisiting Co 2p core-level photoemission in $LiCoO_2$ by in-lab soft and hard X-ray photoelectron spectroscopy: A depth-dependent study of cobalt electronic structure, Surf. Interface Anal. 55 (2023) 489–495.
[73] D. Cabrera-German, G. Gomez-Sosa, A. Herrera-Gomez, Accurate peak fitting and subsequent quantitative composition analysis of the spectrum of Co 2p obtained with Al KÎ± radiation: I: cobalt spinel, Surf. Interface Anal. 48 (2016) 252–256.
[74] J. Yang, H. Liu, W.N. Martens, R.L. Frost, Synthesis and Characterization of Cobalt Hydroxide, Cobalt Oxyhydroxide, and Cobalt Oxide Nanodiscs, J. Phys. Chem. C. 114 (2010) 111–119.
[75] S.C. Petitto, M.A. Langell, Surface composition and structure of Co_3O_4(110) and the effect of impurity segregation, J. Vac. Sci. Technol. A 22 (2004) 1690–1696.
[76] M.A. Golub, E.S. Lopata, L.S. Finney, X-ray Photoelectron Spectroscopy Study of Argon Plasma-Treated Fluoropolymers, Langmuir 10 (1994) 3629–3634.
[77] K. Artyushkova, S. Levendosky, P. Atanassov, J. Fulghum, XPS Structural Studies of Nano-composite Non-platinum Electrocatalysts for Polymer Electrolyte Fuel Cells, Top. Catal. 46 (2007) 263–275.
[78] E.C. Mattson, D.J. Michalak, W. Cabrera, J.F. Veyan, Y.J. Chabal, Initial nitride formation during plasma-nitridation of cobalt surfaces, Appl. Phys. Lett. 109 (2016) 091602.
[79] E.E. Sann, Y. Pan, Z. Gao, S. Zhan, F. Xia, Highly hydrophobic ZIF-8 particles and application for oil-water separation, Sep. Purif. Technol. 206 (2018) 186–191.
[80] Z. Abbasi, E. Shamsaei, X.-Y. Fang, B. Ladewig, H. Wang, Simple fabrication of zeolitic imidazolate framework ZIF-8/polymer composite beads by phase inversion method for efficient oil sorption, J. Colloid Interface Sci. 493 (2017) 150–161.
[81] Y. Ravi, I. Prasanthi, S. Behera, K.K.R. Datta, MIL-101(Fe) Networks Supported on Fluorinated Graphene Nanosheets as Coatings for Oil Sorption, ACS Appl. Nano Mater. 5 (2022) 5857–5867.
[82] D. Kim, D.W. Kim, O. Buyukcakir, M.-K. Kim, K. Polychronopoulou, A. Coskun, Highly Hydrophobic ZIF-8/Carbon Nitride Foam with Hierarchical Porosity for Oil Capture and Chemical Fixation of CO_2, Adv. Funct. Mater. 27 (2017) 1700706.